

LRP 580/97

August 1997

FINITE ELEMENT APPROACH TO GLOBAL GYROKINETIC  
PARTICLE-IN-CELL SIMULATIONS USING MAGNETIC  
COORDINATE

M. Fivaz, S. Brunner, G. De Ridder, O. Sauter,  
T.M. Tran, J. Vaclavik, L. Villard & K. Appert

submitted for publication to  
Computer Physics Communications

# Finite element approach to global gyrokinetic Particle-In-Cell simulations using magnetic coordinates

M. Fivaz, S. Brunner, G. de Ridder, O. Sauter, T. M. Tran,  
J. Vaclavik, L. Villard, K. Appert

Centre de Recherches en Physique des Plasmas,  
Association Euratom-Confédération Suisse,  
Ecole Polytechnique Fédérale de Lausanne,  
PPB, 1015 Lausanne, Switzerland.

## Abstract

We present a fully-global linear gyrokinetic simulation code (GYGLES) aimed at describing the unstable spectrum of the ion-temperature-gradient modes in toroidal geometry. We formulate the Particle-In-Cell method with finite elements defined in magnetic coordinates, which provides excellent numerical convergence properties. The poloidal mode structure corresponding to  $k_{\parallel} = 0$  is extracted without approximation from the equations, which reduces drastically the numerical resolution needed. The code can simulate routinely modes with both very long and very short toroidal wavelengths, can treat realistic (MHD) equilibria of any size and runs on a massively parallel computer.

Email address: fivaz@crpp.epfl.ch

# 1 Introduction

Ion-temperature-gradient-driven turbulence is now commonly thought to play an important role in anomalous radial energy transport in tokamaks; the latter brings one of the main limitations on the performance of current and future tokamaks. Turbulence develops when the plasma equilibrium is linearly unstable; the knowledge of the stability conditions and of the properties of the linear unstable spectrum of the ITG modes is therefore of great interest.

Linear stability in axisymmetric toroidal plasmas, characteristic of tokamaks, is a two-dimensional problem, since each toroidal Fourier harmonic  $n$  can be treated separately. The problem can be treated using the ballooning expansion [1], which is valid at finite magnetic shear and large values of  $n$ . At lowest order, it reduces the number of spatial dimensions to one, a poloidal-like direction. Microinstabilities have been studied extensively with such models [2] [3] [4].

However, the ballooning approximation breaks down at low  $n$ , at low shear, and when the mode is not localized on the outer side of the torus. Even when valid, it can provide only an estimate of the radial structure. Furthermore, the experimentally measured fluctuation spectrum [5] [6] in the TFTR tokamak has been found to be concentrated in very long radial wavelengths; the corresponding modes are therefore of strong interest and require a radially-global approach.

The equations in fully-2D toroidal geometry have been studied by few authors only. In a pioneering work, first results were obtained with a spectral approach [7] [8] [9]. The model does not include finite ions Larmor effects and uses an expansion to second order in banana width, but includes the full trapped electron response. The code, however, must be handled with care to avoid spurious numerical modes. More recently a small number of non-linear gyrokinetic Particle-In-Cell codes have been developed [10] [11] [12]. They showed that in equilibria with large temperature gradients, unstable global modes with strong growth rates and large radial extension develop; in the subsequent nonlinear turbulent phase, the field energy was found to be concentrated in long wavelength modes, which then drive strong anomalous transport. However, the computational cost of these simulations is such that systematic parametric studies such as those needed to study marginal stability conditions are difficult.

We therefore developed simultaneously two new complementary codes to solve efficiently the global linear gyrokinetic kinetic problem: an eigenvalue approach [13] and a time-evolution approach, reported here. This code, GYGLES (GYrokinetic Global LinEar Solver), includes gyrokinetic ions with full banana orbits and Larmor radius effects up to the order of  $(k_{\perp}\rho)^2$ , adiabatic electrons and solves for quasineutral electrostatic perturbations. Three elements give it its originality. First, a Particle-In-Cell method for solving the gyrokinetic equations has been formulated using a finite element representation for the potential, allowing the use of a spatial grid in magnetic coordinates. This provides a fast numerical method that converges very well to the solution of the gyrokinetic equations. Second, the short-wavelength poloidal structure of unstable ITG modes has been extracted without approximation from the equations. This drastically reduces the resolution needed and allows the code to simulate both low- $n$  modes, which are usually in the trapped-ion regime and require the simulation of the full plasma cross section, and high- $n$  modes, which are usually toroidal ITG modes for which the ballooning approximation holds. Third, the code has been coupled with the MHD equilibrium solver CHEASE [14] which allows to study ITG modes in realistic magnetic structures.

To reduce the computing time, the code is run on a massively parallel computer, the Cray T3D. The resulting code allows to find efficiently for any toroidal mode number  $n$  the most unstable mode of a given equilibrium; this is done faster and more precisely than with a nonlinear code. It can routinely treat large realistic toroidal global problems [15].

The remaining of this paper is organized as follows. Section 2 describes the physical model, section 3 the numerical methods, and section 4 the validation of the code, including convergence studies and comparison with other global codes. An example of simulation is shown with the conclusions in section 5.

## 2 The physical model

We focus on the evolution of quasineutral electrostatic perturbations in a plasma modeled by gyrokinetic ions and adiabatic electrons, a model adequate to study ITG stability. This allows to compute whether a given equilibrium configuration is stable for each

toroidal mode number  $n$ . If it is unstable, the system is dominated by the most unstable mode after a finite time-evolution. By looking at the electrostatic potential and its time evolution, we can then compute the frequency, growth rate and spatial structure of the most unstable mode.

## 2.1 Definitions and coordinate system

We study axisymmetric equilibria, associated naturally with a cylindrical coordinate system  $(R, \varphi, Z)$ . The magnetic field  $\mathbf{B}(\mathbf{x})$ , like any axisymmetric and divergence-free vector field, can be written as:

$$\mathbf{B} = T(\Psi)\nabla\varphi + \nabla\Psi \times \nabla\varphi \quad (1)$$

where  $\Psi$  is a function of  $R$  and  $Z$  only and, to an arbitrary additive constant, is the magnetic flux that goes through the disc  $\{(R, \varphi, Z), \varphi = [0, 2\pi]\}$  perpendicular to the axis of symmetry. The direction of the magnetic field is  $\mathbf{h} = \mathbf{B}/B$ . Since  $\mathbf{B} \cdot \nabla\Psi = 0$ , the magnetic field lines lie on the surfaces of constant magnetic flux; these are called magnetic surfaces. There is a magnetic axis on the innermost surface at  $(R = R_M, Z = 0)$  where  $\nabla\Psi(R_M, 0) = 0$  and the magnetic field is purely toroidal. The additive constant that may be added to  $\Psi$  is chosen so that  $\Psi = 0$  on the magnetic axis. A magnetic spatial coordinate system is given by  $(s, \varphi, \theta)$ , such that

$$\tan \theta = \frac{Z}{R - R_M} \quad \text{and} \quad s = \sqrt{\frac{\Psi}{\Psi_a}} \quad (2)$$

where  $\Psi_a$  is the value of  $\Psi$  at the plasma edge;  $s$  acts as a radial variable and  $\theta$  is a poloidal angle.

The plasma at equilibrium is assumed to be free of flow and of electric field. The equilibrium electron density is assumed equal to the ion density  $n_0(s)$ . The electron and ion temperatures are  $T_e(s)$  and  $T_i(s)$ ; the Boltzmann constant will be omitted everywhere. The ion thermal velocity is  $v_{thi}(s) = \sqrt{T_i(s)/m_i}$ , and the MHD pressure is  $p(s)$ . The inverse scale lengths of  $n_0$  and  $T_i$  are given respectively by

$$\frac{1}{L_n} = |\nabla \ln n_0|, \quad \frac{1}{L_T} = |\nabla \ln T_i| \quad (3)$$

The ion cyclotron frequency is given by  $\Omega = q_i B/m_i$ , where  $q_i$  and  $m_i$  are the ion charge and mass.

The quantities associated with the perturbations to the equilibrium are noted in the following way. The electron and ion density perturbations are  $n_e(\mathbf{x})$  and  $n_i(\mathbf{x})$ , and induce an electric field  $\mathbf{E}(\mathbf{x})$  and an electrostatic potential  $\phi(\mathbf{x})$ . We denote as  $\mathbf{k}$  the perturbation wavevector,  $k_{\parallel}$  and  $k_{\perp}$  its parallel and perpendicular components,  $n$  the toroidal mode number associated with  $\varphi$ ,  $m$  the poloidal mode number associated with  $\theta$ , and  $\omega$  the frequency of the perturbation.

The MKSA unit system is used throughout.

## 2.2 Gyrokinetic model for ions

We describe the plasma ions with a gyrokinetic model obtained by averaging out the fast cyclotron motion from a Vlasov-Poisson system. In the derivation from Ref. [16], the phase-space Lagrangian variation method and the Lie perturbation theory are utilized in order to preserve the Hamiltonian structure of the original Vlasov-Poisson model. The usual gyrokinetic ordering is used:  $\omega/\Omega \sim k_{\parallel}/k_{\perp} \sim e\phi/T_e \sim \rho/L_n \sim \rho/L_T \sim \mathcal{O}(\epsilon_g)$ , where  $\rho$  is the ion Larmor radius. A second small parameter is  $\rho/L_B \sim \mathcal{O}(\epsilon_B)$ , with  $L_B = B/|\nabla B|$ . The equations are valid up to  $\mathcal{O}(\epsilon_g^2)$ ,  $\mathcal{O}(\epsilon_g\epsilon_B)$  and  $\mathcal{O}(\epsilon_B)$ .

In this regime, the particle guiding centers are well defined. Let  $\mathbf{R}$  be the position of a particle guiding center,  $\mathbf{x}$  the particle position, and  $\boldsymbol{\rho} = \mathbf{x} - \mathbf{R}$  the Larmor radius vector. One can define two orthonormal vectors  $\mathbf{e}_{\perp 1}$  and  $\mathbf{e}_{\perp 2}$  that are perpendicular to the magnetic field in  $\mathbf{R}$ ; one then has:

$$\boldsymbol{\rho}(\mathbf{R}, v_{\perp}, \alpha) = \frac{v_{\perp}}{\Omega(\mathbf{R})}(\mathbf{e}_{\perp 1} \cos \alpha + \mathbf{e}_{\perp 2} \sin \alpha) \quad (4)$$

where  $v_{\parallel}$  and  $v_{\perp}$  are the components of the particle velocity that are parallel and perpendicular to the magnetic field, and where  $\alpha$  is the gyroangle. The gyrokinetic equations describe the evolution of the guiding center distribution  $f(\mathbf{R}, v_{\parallel}, v_{\perp})$ ; the dependence in the gyroangle  $\alpha$  has been averaged out.

### 2.2.1 Original equations

In our notation, using the variable  $v_\perp$  instead of  $M = m_i v_\perp^2 / 2\Omega$ , the equations from [16] become:

$$\frac{d\mathbf{R}}{dt} = v_\parallel \mathbf{h} + \frac{v_\parallel^2 + v_\perp^2 / 2}{\Omega} \mathbf{h} \times \frac{\nabla B}{B} - \frac{v_\parallel^2}{\Omega} \mathbf{h} \times \left[ \mathbf{h} \times \frac{\nabla \times \mathbf{B}}{B} \right] + \frac{\langle \mathbf{E} \rangle \times \mathbf{B}}{B^2} \quad (5)$$

$$\frac{dv_\parallel}{dt} = \frac{1}{2} v_\perp^2 \nabla \cdot \mathbf{h} + \frac{q_i}{m_i} \mathbf{h} \cdot \langle \mathbf{E} \rangle + \frac{v_\parallel}{B} \mathbf{h} \times \frac{\nabla B}{B} \cdot \langle \mathbf{E} \rangle - \frac{v_\parallel}{B} \mathbf{h} \times \left[ \mathbf{h} \times \frac{\nabla \times \mathbf{B}}{B} \right] \cdot \langle \mathbf{E} \rangle \quad (6)$$

$$\frac{dv_\perp}{dt} = -\frac{1}{2} v_\perp v_\parallel \nabla \cdot \mathbf{h} + \frac{v_\perp}{2B} \mathbf{h} \times \frac{\nabla B}{B} \cdot \langle \mathbf{E} \rangle \quad (7)$$

$$\frac{\partial f}{\partial t} + \frac{d\mathbf{R}}{dt} \frac{\partial f}{\partial \mathbf{R}} + \frac{dv_\parallel}{dt} \frac{\partial f}{\partial v_\parallel} + \frac{dv_\perp}{dt} \frac{\partial f}{\partial v_\perp} = 0 \quad (8)$$

$$n_i(\mathbf{x}) = \int \left[ f(\mathbf{R}, v_\parallel, v_\perp) + \frac{q_i}{m_i v_\perp} (\phi(\mathbf{x}) - \langle \phi \rangle(\mathbf{R}, v_\perp)) \frac{\partial f(\mathbf{R}, v_\parallel, v_\perp)}{\partial v_\perp} \right] \delta(\mathbf{R} - \mathbf{x} + \boldsymbol{\rho}) d\mathbf{R} dv \quad (9)$$

$$\langle \phi \rangle(\mathbf{R}, v_\perp) = \frac{1}{2\pi} \int \phi(\mathbf{x}) \delta(\mathbf{R} - \mathbf{x} + \boldsymbol{\rho}) d\mathbf{x} d\alpha \quad (10)$$

$$\langle \mathbf{E} \rangle(\mathbf{R}, v_\perp) = -\nabla \langle \phi \rangle(\mathbf{R}, v_\perp) \quad (11)$$

Here,  $d\mathbf{x}$ ,  $d\mathbf{R}$  and  $d\mathbf{v}$  are associated with the integration over configuration and velocity space. The nonlinear terms in the electric field equation (11) have been left out. In each equation, the leading order terms only have been kept:  $B^* = B + v_\parallel \frac{m_i}{q_i} \mathbf{h} \cdot \nabla \times \mathbf{h}$  has been replaced by  $B$  and the term in  $\mathcal{O}(\epsilon_g^2)$  in the density equation (9) has been left out.

Equation (8) can also be written as the total derivative of  $f$  along the guiding center trajectories:

$$\frac{d}{dt} f(\mathbf{R}(t), v_\parallel(t), v_\perp(t)) = 0 \quad (12)$$

with the guiding center trajectories  $(\mathbf{R}(t), v_\parallel(t), v_\perp(t))$  defined by Eqs. (5-7) for every possible initial condition.

We shall treat the problem perturbatively. We first look for a stationary axisymmetric solution  $f_0$  of the equations, associated with a constant potential  $\phi_0 = 0$ . We set  $f = f_0 + \epsilon_a \tilde{f}$  and  $\phi = \phi_0 + \epsilon_a \tilde{\phi}$ , where  $\epsilon_a$  is a small parameter proportional to the amplitude of the perturbation of the stationary solution. We then expand the equations to first order in  $\epsilon_a$  to obtain the evolution of the perturbations  $\tilde{f}$  and  $\tilde{\phi}$ .

To simplify notation, we now suppress the tildes over the perturbed quantities.

### 2.2.2 Ion equilibrium distribution

We first need a stationary solution of equation (12). Since we consider equilibria free of electric field, the guiding center trajectories are given by Eqs. (5) to (7) with  $\langle \mathbf{E} \rangle = 0$ . One can easily verify that these trajectories have three constants of motion: the kinetic energy  $\epsilon = \frac{1}{2}m(v_{\parallel}^2 + v_{\perp}^2)$ , the magnetic moment  $M = mv_{\perp}^2/2\Omega$  and the toroidal canonical angular momentum  $\Psi_0 = \Psi + \frac{m_i}{q_i}Rv_{\parallel}h_{\varphi}$ . Any arbitrary function  $f_0$  of the constants of motion is a stationary solution:

$$\frac{d}{dt}f_0(\epsilon, M, \Psi_0) = \frac{d\epsilon}{dt}\frac{\partial f_0}{\partial \epsilon} + \frac{dM}{dt}\frac{\partial f_0}{\partial M} + \frac{d\Psi_0}{dt}\frac{\partial f_0}{\partial \Psi_0} = 0 \quad (13)$$

Expanding  $f_0(\Psi_0)$  around  $\Psi$ , one gets:

$$f_0(\Psi_0) = f_0(\Psi) + \frac{\partial f_0}{\partial \Psi}(\Psi_0 - \Psi) \quad (14)$$

The second term is smaller than the first by a factor ( $\rho/L_n \sim \epsilon_g$ ) and can be neglected; we therefore take  $f_0$  as a function of  $\Psi$  instead of  $\Psi_0$ , or equivalently as a function of  $s$ . Choosing two free functions, the ion guiding centers density  $n_0(s)$  and temperature  $T_i(s)$ , we define  $f_0$  as a local Maxwellian:

$$f_0(\epsilon, s) = \frac{n_0(s)}{(2\pi)^{3/2}v_{thi}^3(s)} \exp\left\{-\frac{1}{2}\frac{v_{\parallel}^2 + v_{\perp}^2}{v_{thi}^2(s)}\right\} \quad (15)$$

### 2.2.3 Linearization of the ion response

We now carry the expansion in perturbation amplitude, writing Eqs. (12) and (9) to first order in  $\epsilon_a$ :

$$\frac{d\mathbf{R}}{dt} = v_{\parallel}\mathbf{h} + \frac{v_{\parallel}^2 + v_{\perp}^2/2}{\Omega}\mathbf{h} \times \frac{\nabla B}{B} - \frac{v_{\parallel}^2}{\Omega}\mathbf{h} \times \left[\mathbf{h} \times \frac{\nabla \times \mathbf{B}}{B}\right] \quad (16)$$

$$\frac{dv_{\parallel}}{dt} = \frac{1}{2}v_{\perp}^2\nabla \cdot \mathbf{h} \quad , \quad \frac{dv_{\perp}}{dt} = -\frac{1}{2}v_{\perp}v_{\parallel}\nabla \cdot \mathbf{h} \quad (17)$$

$$\frac{d}{dt}f(\mathbf{R}(t), v_{\parallel}(t), v_{\perp}(t)) = \mathcal{T}(\mathbf{E}) \quad (18)$$

$$\begin{aligned} \mathcal{T}(\mathbf{E}) = & -\frac{\langle \mathbf{E} \rangle \times \mathbf{B}}{B^2} \frac{\partial f_0}{\partial \mathbf{R}} - \frac{q_i}{m_i} \mathbf{h} \cdot \langle \mathbf{E} \rangle \frac{\partial f_0}{\partial v_{\parallel}} \\ & - \left( v_{\parallel} \frac{\partial f_0}{\partial v_{\parallel}} + \frac{1}{2} v_{\perp} \frac{\partial f_0}{\partial v_{\perp}} \right) \langle \mathbf{E} \rangle \cdot \mathbf{h} \times \frac{\nabla B}{B^2} \\ & + \frac{v_{\parallel}}{B} \mathbf{h} \times \left[ \mathbf{h} \times \frac{\nabla \times \mathbf{B}}{B} \right] \cdot \langle \mathbf{E} \rangle \frac{\partial f_0}{\partial v_{\parallel}} \end{aligned} \quad (19)$$



The density equation (9) becomes:

$$n_i(\mathbf{x}) = \int \left[ f(\mathbf{R}, v_{\parallel}, v_{\perp}) + \frac{q_i}{m_i v_{\perp}} (\phi - \langle \phi \rangle) \frac{\partial f_0}{\partial v_{\perp}} \right] \delta(\mathbf{R} - \mathbf{x} + \boldsymbol{\rho}) d\mathbf{R} dv \quad (20)$$

#### 2.2.4 Long wavelength approximation for the polarization density

The second term in Eq. (20) is the polarization density, which depends on the potential through an integral over the equilibrium distribution function  $f_0$ . The integral kernel has a correlation length of the order of the Larmor radius. Since wavelengths longer than the Larmor radius are those which seem to lead to the highest values of anomalous transport, one can assume  $k_{\perp} \rho \ll 1$  without losing the correct description of the most important modes.

By expanding the delta functions around  $\mathbf{R} - \mathbf{x}$  in (10) and in the second term of (20) to second order in  $\boldsymbol{\rho}$  and performing the integrals over all the velocity variables, including the gyroangle, one gets a differential expression for  $n_i$  that is valid to the order of  $(k_{\perp} \rho)^2$ :

$$n_i(\mathbf{x}) = \int f(\mathbf{R}, v_{\parallel}, v_{\perp}) \delta(\mathbf{R} - \mathbf{x} + \boldsymbol{\rho}) d\mathbf{R} dv + \nabla_{\perp} \cdot \left[ \frac{n_0}{B\Omega} \nabla_{\perp} \phi(\mathbf{x}) \right] \quad (21)$$

### 2.3 Model for electrons and closure

The quasineutrality constraint  $n_e = n_i$  is used. The electrons are assumed to be bound to and to respond adiabatically within their magnetic surface. For small electron density perturbations  $n_e$ , we get:

$$n_i(\mathbf{x}) = n_e(\mathbf{x}) = \frac{en_0(s)}{T_e(s)} (\phi(\mathbf{x}) - \bar{\phi}(s)) \quad (22)$$

where  $-e$  is the electron charge and  $\bar{\phi}(s)$  is the magnetic surface average of  $\phi(\mathbf{x})$ . The second term is non-zero for axisymmetric ( $n=0$ ) perturbations only. It can be dropped, since we will not consider such perturbations.

This closes our system of equations by providing an equation for the electrostatic potential.

## 2.4 Consistent MHD equilibrium

The functions  $\Psi$  and  $T(\Psi)$  that appear in the expression for the magnetic field, Eq. (1), are given either by an ad-hoc functions or by a numerical solution of the Grad-Shafranov equation computed by the code CHEASE [14]. In that case, we use consistent kinetic equilibria  $f_0$  and MHD equilibria: the pressure profile that determines  $\Psi$  through the Grad-Shafranov equation is related straightforwardly to the density and temperature profiles that determine  $f_0$ , Eq. (15):

$$p(s) = n_i(s) (T_e(s) + T_i(s)) \quad (23)$$

This coupling introduces an interesting dependence on the value of the density: without (23), the density appears only through its logarithmic gradient, which is insensitive to a multiplication by a constant. The finite-pressure stabilization of ITG modes (or second stability region) occurs at high density [17] [18].

## 2.5 Toroidal Fourier transform

Since the equations are linear and the equilibrium is homogeneous in the toroidal direction, every toroidal Fourier harmonic  $n$  is independent. Choosing one value of  $n$ , we define transformed quantities, denoted by a tilde ( $\tilde{\phantom{x}}$ ):

$$f(R, \varphi, Z, v_{\parallel}, v_{\perp}) = \tilde{f}(R, Z, v_{\parallel}, v_{\perp}) e^{iS(R, \varphi, Z)} \quad (24)$$

$$\phi(R, \varphi, Z) = \tilde{\phi}(R, Z) e^{iS(R, \varphi, Z)} \quad (25)$$

$$S(R, \varphi, Z) = \Sigma(R, Z) - n\varphi. \quad (26)$$

At this point, we take  $\Sigma(R, Z) = 0$ , and the transformation reduces to a simple Fourier transform. Later,  $\Sigma$  will be used to split off from  $f$  a fast variation in  $R$  and  $Z$ ; the development that follows is valid for arbitrary functions  $\Sigma(R, Z)$ .

Defining  $\mathbf{K} = \nabla S$  and noting that  $\frac{d}{dt} S = \mathbf{K} \cdot \frac{d}{dt} \mathbf{R}$ , we get:

$$\frac{d\tilde{f}}{dt} + i \frac{dS}{dt} \tilde{f} = \tilde{\mathcal{T}}(\tilde{\mathbf{E}}), \quad (27)$$

$$\begin{aligned}
\tilde{\mathcal{T}}(\tilde{\mathbf{E}}) = & -\frac{\langle \tilde{\mathbf{E}} \rangle \times \mathbf{B}}{B^2} \frac{\partial f_0}{\partial \mathbf{R}} - \frac{q_i}{m_i} \mathbf{h} \cdot \langle \tilde{\mathbf{E}} \rangle \frac{\partial f_0}{\partial v_{\parallel}} \\
& - \left( v_{\parallel} \frac{\partial f_0}{\partial v_{\parallel}} + \frac{1}{2} v_{\perp} \frac{\partial f_0}{\partial v_{\perp}} \right) \langle \tilde{\mathbf{E}} \rangle \cdot \mathbf{h} \times \frac{\nabla B}{B^2} \\
& + \frac{v_{\parallel}}{B} \mathbf{h} \times \left[ \mathbf{h} \times \frac{\nabla \times \mathbf{B}}{B} \right] \cdot \langle \tilde{\mathbf{E}} \rangle \frac{\partial f_0}{\partial v_{\parallel}}
\end{aligned} \tag{28}$$

$$\tilde{n}_i(\mathbf{x}) = \int \tilde{f}(\mathbf{R}, v_{\parallel}, v_{\perp}) \delta(\mathbf{R} - \mathbf{x} + \boldsymbol{\rho}) e^{iS(\mathbf{R}) - iS(\mathbf{x})} d\mathbf{R} dv \tag{29}$$

$$\begin{aligned}
& + (i\mathbf{K}_{\perp} + \nabla_{\perp}) \cdot \frac{n_0}{B\Omega} (i\mathbf{K}_{\perp} + \nabla_{\perp}) \tilde{\phi}(\mathbf{x}) \\
\langle \tilde{\mathbf{E}} \rangle(\mathbf{R}, v_{\perp}) = & - \int \left[ (i\mathbf{K} + \nabla) \tilde{\phi}(\mathbf{x}) \right] \delta(\mathbf{x} - \mathbf{R} + \boldsymbol{\rho}) e^{iS(\mathbf{x}) - iS(\mathbf{R})} d\mathbf{x} dv.
\end{aligned} \tag{30}$$

The toroidal angle  $\varphi$  now appears only in  $S(\mathbf{x})$  and  $S(\mathbf{R})$ . However, the phase difference  $S(\mathbf{x}) - S(\mathbf{R})$ , which is related to the toroidal component of the Larmor radius, does not depend on  $\varphi$ . We note that  $\nabla_{\perp}$  and  $\nabla$  operate on quantities that do not depend on  $\varphi$ , and that their component along  $\nabla\varphi$  has been removed into the vector  $\mathbf{K}$ . The tildes over the transformed quantities will be omitted hereafter.

## 2.6 Final equations

Incorporating all the elements developed above, one obtains the final equations of our model.

- Unperturbed guiding center trajectories:

$$\frac{d\mathbf{R}}{dt} = v_{\parallel} \mathbf{h} + \frac{v_{\parallel}^2 + v_{\perp}^2/2}{\Omega} \mathbf{h} \times \frac{\nabla B}{B} - \frac{v_{\parallel}^2}{\Omega} \mathbf{h} \left[ \times \mathbf{h} \times \frac{\nabla \times \mathbf{B}}{B} \right] \tag{31}$$

$$\frac{dv_{\parallel}}{dt} = \frac{1}{2} v_{\perp}^2 \nabla \cdot \mathbf{h}, \quad \frac{dv_{\perp}}{dt} = -\frac{1}{2} v_{\perp} v_{\parallel} \nabla \cdot \mathbf{h} \tag{32}$$

- Evolution of the perturbed distribution function along the unperturbed guiding center trajectories:

$$\frac{df}{dt} + i \frac{dS}{dt} f = \mathcal{T}(\mathbf{E}), \tag{33}$$

$$\begin{aligned}
\mathcal{T}(\mathbf{E}) = & -\frac{\langle \mathbf{E} \rangle \times \mathbf{B}}{B^2} \frac{\partial f_0}{\partial \mathbf{R}} - \frac{q_i}{m_i} \mathbf{h} \cdot \langle \mathbf{E} \rangle \frac{\partial f_0}{\partial v_{\parallel}} \\
& - \left( v_{\parallel} \frac{\partial f_0}{\partial v_{\parallel}} + \frac{1}{2} v_{\perp} \frac{\partial f_0}{\partial v_{\perp}} \right) \langle \mathbf{E} \rangle \cdot \mathbf{h} \times \frac{\nabla B}{B^2} \\
& + \frac{v_{\parallel}}{B} \mathbf{h} \times \mathbf{h} \times \frac{\nabla \times \mathbf{B}}{B} \cdot \langle \mathbf{E} \rangle \frac{\partial f_0}{\partial v_{\parallel}}
\end{aligned} \tag{34}$$

- Self-consistent electrostatic potential and the gyro-averaged electric field:

$$\frac{n_0 e}{T_e} \phi(\mathbf{x}) - (i\mathbf{K}_{\perp} + \nabla_{\perp}) \cdot \frac{n_0}{B\Omega} (i\mathbf{K}_{\perp} + \nabla_{\perp}) \phi(\mathbf{x}) = \tag{35}$$

$$= \int f(\mathbf{R}, v_{\parallel}, v_{\perp}) \delta(\mathbf{R} - \mathbf{x} + \boldsymbol{\rho}) e^{iS(\mathbf{R}) - iS(\mathbf{x})} d\mathbf{R} d\mathbf{v}$$

$$\langle \mathbf{E} \rangle(\mathbf{R}, v_{\perp}) = -\frac{1}{2\pi} \int [(i\mathbf{K} + \nabla) \phi(\mathbf{x})] \delta(\mathbf{x} - \mathbf{R} + \boldsymbol{\rho}) e^{iS(\mathbf{x}) - iS(\mathbf{R})} d\mathbf{x} d\alpha. \tag{36}$$

- The vector  $\mathbf{K}$  is given by the gradient of  $S$ , Eq. (26),  $f_0$  by Eq. (15),  $\boldsymbol{\rho}$  by Eq. (4) and the magnetic field  $\mathbf{B}$  by Eq. (1). Both  $d\mathbf{R} = dR dZ R d\varphi$  and  $d\mathbf{x} = dR_x dZ_x R_x d\varphi_x$  are related to the integration over configuration space and  $d\mathbf{v} = dv_{\parallel} dv_{\perp} v_{\perp} d\alpha$  to the integration over velocities.
- An equilibrium is fully specified by four free functions: the density  $n_0(s)$  and the ion and electron temperatures  $T_e(s)$  and  $T_i(s)$  determine the equilibrium distribution function. A fourth function is needed, in addition to Eq. (23), to determine the magnetic field, Eq. (1), through the Grad-Shafranov equation. We usually specify either the surface-averaged current density or the current flux  $T(\Psi)$ .

### 3 Numerical resolution with a finite element PIC method

We shall solve the system of equations derived in the previous section by integrating the perturbed distribution function  $f$ , Eq. (33), along the unperturbed trajectories of the guiding centers, Eqs. (31) and (32) using the source  $\mathcal{T}(\mathbf{E})$  from Eq. (34). This source depends on the self-consistent electric field given by Eqs. (35) and (36). This is performed numerically with a finite element Particle-In-Cell method presented in this section.

We represent the potential on a grid that is aligned with the magnetic surfaces; this has several advantages. First, the radial and poloidal resolutions can be chosen independently and adapted to the mode simulated. Typical mode structures are then reproduced with relatively few grid points, and the particle noise, which is proportional to the square root of the number of particles per cell, is consequently low. Second, it allows, when appropriate, to discretize only the radial interval where the mode is localized; this interval is usually much smaller than the plasma minor radius. Third, it allows to filter out the poloidal harmonics that correspond to high values of  $k_{\parallel}$  and whose amplitudes are known to be small in unstable modes.

Complex geometries are difficult to deal with using standard PIC schemes, but are handled naturally within the framework of finite elements. If the finite element PIC method [19] [20] is applied to a 1D slab Vlasov-Poisson model using linear finite elements, one obtains a standard energy conserving scheme. With elements of higher order, the scheme obtained also conserves energy in time and the solution of the field equation has a higher order spatial convergence. Finite element PIC schemes can therefore be seen as generalizations of standard energy-conserving schemes which allow complex geometries to be used and have good spatial convergence properties. The finite element method is not prone to the numerical instabilities described in [21]; it also allows to solve the field equation (35) without approximation, contrarily to the usual simple Fourier methods where the coefficients of the equation are assumed constant and where a Cartesian operator replaces the correct cylindrical one [11] [12].

We also use a flexible phase space discretization scheme that allows to “pack” the par-

ticles in phase space. The resulting scheme is very efficient in term of the number of particles and grid points required for a given accuracy.

### 3.1 Discretization of the distribution function

The ion distribution function  $f$  has to be discretized in a four-dimensional reduced phase space  $(R, Z, v_{\parallel}, v_{\perp})$ , the toroidal angle  $\varphi$  and the gyroangle  $\alpha$  having been treated analytically. The Jacobian in the reduced phase space is  $J = (2\pi)^2 R v_{\perp}$ .

The initial distribution function is discretized in the reduced phase space domain limited by  $[s_{min}^f < s < s_{max}^f]$ ,  $[0 \leq \theta < 2\pi]$  and  $[v_{\perp}^2 + v_{\parallel}^2 < \kappa_v v_{thi}^2]$ , where  $s_{max}^f$ ,  $s_{min}^f$  and  $\kappa_v$  are numerical parameters to be chosen. This domain is partitioned into  $N_p$  subdomains which are referred to by the subscript  $\nu$ . Each has a phase space volume noted  $\xi_{\nu}$  and is centered initially on the coordinates  $(R_{\nu}, Z_{\nu}, v_{\parallel\nu}, v_{\perp\nu})$ . The subdomains can be concentrated where the distribution function is expected to be maximum or highly structured. The distribution function is then discretized in the following way:

$$f(R, Z, v_{\parallel}, v_{\perp}, t) = \sum_{\nu} \frac{f_{\nu}(t)}{J} \delta^{pol}(\mathbf{R} - \mathbf{R}_{\nu}(t)) \delta(v_{\parallel} - v_{\parallel\nu}(t)) \delta(v_{\perp} - v_{\perp\nu}(t)) \quad (37)$$

where  $\delta^{pol}(\mathbf{R}) \equiv \delta(R)\delta(Z)$  denotes a delta function in the poloidal plane. The weights  $f_{\nu}(t)$  represent the perturbed number of ions in the phase space volume  $\xi_{\nu}$  and the local value of the distribution function is given by  $f_{\nu}/\xi_{\nu}$ . We refer to the  $N_p$  subdomains as  $N_p$  gyrocenter "particles"; the center of each domain  $(R_{\nu}, Z_{\nu}, v_{\parallel\nu}, v_{\perp\nu})$  is the particle position in reduced phase space,  $\xi_{\nu}$  the phase space volume carried by each particle, and  $f_{\nu}$  the particle weight.

Since the flow of guiding centers in phase space is incompressible, the phase space volume  $\xi_{\nu}$  carried by a particle is constant in time, though its shape changes. Therefore, inserting (37) into (33) and integrating in phase space over  $\xi_{\nu}$  yields, since  $\xi_{\nu}$  commutes with  $\frac{d}{dt}$  on the left hand side:

$$\left. \frac{df_{\nu}}{dt} + i \frac{dS}{dt} \right|_{\nu} f_{\nu} = \mathcal{T}(\mathbf{E})|_{\nu} \xi_{\nu} \quad (38)$$

The particle positions in reduced phase space  $(R_{\nu}(t), Z_{\nu}(t), v_{\parallel\nu}(t), v_{\perp\nu}(t))$  are evolved in time with Eqs. (31) and (32). One therefore has a scheme that solves Eq. (33): the value of the distribution function along the unperturbed guiding center trajectories varies with the source  $\mathcal{T}(\mathbf{E})$ .

Particles that leave the plasma are eliminated. As they carry only the perturbation of the distribution function, this is equivalent to neglecting the perturbation along the orbits that are not fully inside the plasma.

## 3.2 Discretization of the electrostatic potential with finite elements

### 3.2.1 The mesh and the finite elements

The finite elements chosen are splines, which are commonly used in Particle-In-Cell simulations. Their usefulness stems from their robustness in avoiding sub-grid-scale oscillations, and from the property that:

$$\sum_j \mathcal{S}^p(s + j\Delta s) = 1 \quad (39)$$

for any value of  $s$ , where  $\mathcal{S}^p(s)$  is a spline of order  $p$  and of length  $(p + 1)\Delta s$ . This ensures that the total charge associated with a particle is independent of its position with respect to the mesh.

Let  $j$  and  $i$  cover the intervals  $[1, \dots, n_s]$  and  $[1, \dots, n_\theta]$  in what follows. We define a two-dimensional mesh in  $(s, \theta)$  of  $n_s \times n_\theta$  points, with  $0 \leq s_{min} < s_{max} \leq 1$ , Fig. (1):

$$\begin{aligned} s_j &= s_{min} + (j - 1)\Delta s, & \Delta s &= \frac{s_{max} - s_{min}}{n_s - 1}, \\ \theta_i &= (i - 1)\Delta\theta, & \Delta\theta &= \frac{2\pi}{n_\theta - 1}, \end{aligned} \quad (40)$$

Let  $L_j(s)$  be  $n_s$  linear splines, centered respectively on  $s_j$ , and  $\{L_i(\theta)\}$  be  $n_\theta$  periodic linear splines, centered respectively on  $\theta_i$ . We define similarly two sets of quadratic splines  $\{Q_j(s)\}$  and  $\{Q_i(\theta)\}$ , Fig. (2), centered respectively on  $s_{j+1/2}$  and on  $\theta_{i+1/2}$  [19]. A two-dimensional basis for the discrete potential is built either with the linear (41) or the quadratic (42) splines:

$$\Lambda_k(s, \theta) = L_j(s)L_i(\theta), \quad k = i + n_\theta(j - 1), \quad k = [1, \dots, n_s n_\theta] \quad (41)$$

$$\Lambda_k(s, \theta) = Q_j(s)Q_i(\theta), \quad k = i + n_\theta(j - 1), \quad k = [1, \dots, n_s n_\theta] \quad (42)$$

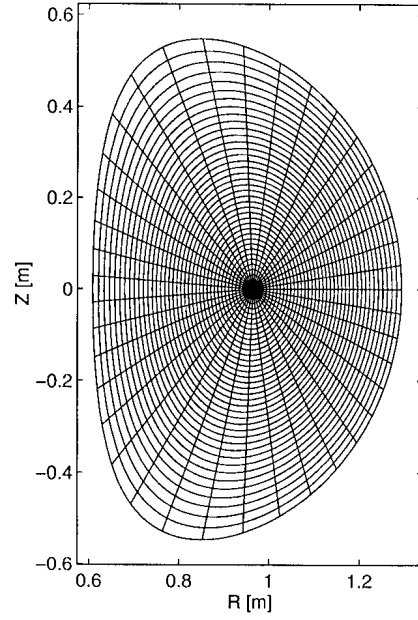


Figure 1: *Grid aligned with magnetic surfaces for the representation of the potential*

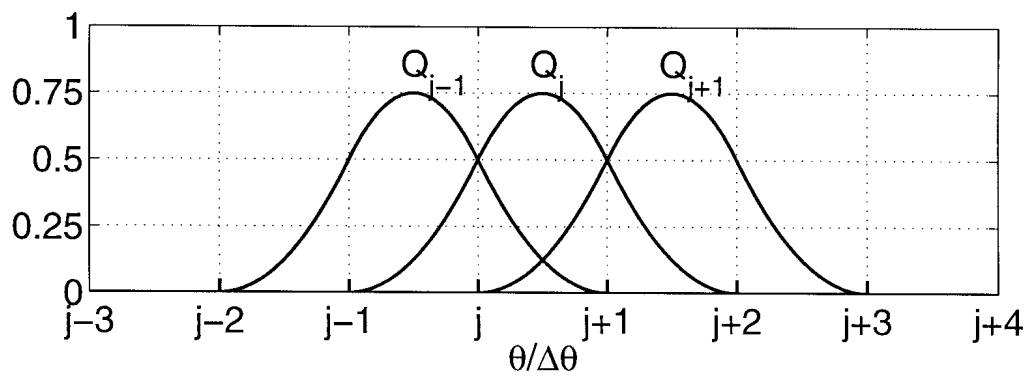


Figure 2: *Set of quadratic splines in  $\theta$*



### 3.2.2 Representation of the potential

The potential is represented on this finite element basis by:

$$\phi(\mathbf{x}) = \sum_k \phi_k \Lambda_k(\mathbf{x}) \quad (43)$$

Inserting (37) and (43) into the field equation (35) and performing the integrals over  $v_{\parallel}$  and  $v_{\perp}$  (but not over  $\alpha$ ) on the right hand side, one gets:

$$\begin{aligned} & \sum_k \phi_k \left[ \frac{n_0 e}{T_e} \Lambda_k(\mathbf{x}) - (i\mathbf{K}_{\perp} + \nabla_{\perp}) \cdot \frac{n_0}{B\Omega} (i\mathbf{K}_{\perp} + \nabla_{\perp}) \Lambda_k(\mathbf{x}) \right] \\ &= \sum_{\nu} \int \frac{f_{\nu}}{(2\pi)^2 R} \delta^{pol}(\mathbf{R} - \mathbf{R}_{\nu}) \delta(\mathbf{R} - \mathbf{x} + \boldsymbol{\rho}_{\nu}) e^{iS(\mathbf{R}) - iS(\mathbf{x})} d\mathbf{R} d\alpha \end{aligned} \quad (44)$$

where  $\boldsymbol{\rho}_{\nu}$  is the Larmor radius for the particle  $\nu$ . Multiplying this equation by an element  $\Lambda_l(\mathbf{x})$ ,  $l = 1, \dots, n_s n_{\theta}$  and integrating over space yields:

$$\begin{aligned} & \sum_k \phi_k \int \left[ \frac{n_0 e}{T_e} \Lambda_k(\mathbf{x}) - (i\mathbf{K}_{\perp} + \nabla_{\perp}) \cdot \frac{n_0}{B\Omega} (i\mathbf{K}_{\perp} + \nabla_{\perp}) \Lambda_k(\mathbf{x}) \right] \Lambda_l(\mathbf{x}) d\mathbf{x} = \\ &= \sum_{\nu} \int \frac{f_{\nu}}{(2\pi)^2 R} \delta^{pol}(\mathbf{R} - \mathbf{R}_{\nu}) \delta(\mathbf{R} - \mathbf{x} + \boldsymbol{\rho}_{\nu}) e^{iS(\mathbf{R}) - iS(\mathbf{x})} \Lambda_l(\mathbf{x}) d\mathbf{x} d\mathbf{R} d\alpha \end{aligned} \quad (45)$$

or, in matrix form, after integration of the delta functions and integration by parts of the  $\nabla_{\perp}$  term:

$$\sum_k M_{lk} \phi_k = N_l \quad (46)$$

$$M_{lk} = \int \left\{ \frac{n_0 e}{T_e} \Lambda_k(\mathbf{x}) \Lambda_l(\mathbf{x}) + \frac{n_0}{B\Omega} [(i\mathbf{K}_{\perp} + \nabla_{\perp}) \Lambda_k(\mathbf{x})] \cdot [(-i\mathbf{K}_{\perp} + \nabla_{\perp}) \Lambda_l(\mathbf{x})] \right\} d\mathbf{x} \quad (47)$$

$$N_l = \sum_{\nu} \frac{f_{\nu}}{2\pi} \int \Lambda_l(\mathbf{R}_{\nu} + \boldsymbol{\rho}_{\nu}) e^{iS(\mathbf{R}_{\nu}) - iS(\mathbf{R}_{\nu} + \boldsymbol{\rho}_{\nu})} d\alpha \quad (48)$$

The computation of the vector  $\mathbf{N}$  is called “charge assignment” in Particle-In-Cell methods, because it assigns to the mesh the charge associated with the distribution function. It appears naturally within the finite element formulation. The finite element matrix  $\mathbf{M}$  is complex, hermitian and positive definite. Once the charge assignment is done, the coefficients  $\phi_l$  are computed by solving the linear problem (46). This is achieved by performing first a Choleski decomposition, followed by a back-substitution [22]. Since the matrix does not vary in time, it is built and decomposed once only at the beginning

of the simulation. The back-substitution provides the solution very efficiently at each time step.

The boundary conditions on  $\phi$  are periodic in  $\theta$ . Radially, for all values of  $\theta$ , we impose  $\phi(s_{max}, \theta) = \phi(s_{min}, \theta) = 0$ , unless  $s_{min} = 0$ ; in that case, we require that  $\phi(s = 0, \theta = [0, 2\pi])$  has a unique value.

### 3.2.3 Electric field

The gyro-averaged electric field (36) becomes, integrating the delta functions:

$$\langle \mathbf{E} \rangle(\mathbf{R}, v_{\perp}) = - \sum_k \frac{\phi_k}{2\pi} \int [i\mathbf{K}\Lambda_k(\mathbf{R} - \boldsymbol{\rho}) + \nabla\Lambda_k(\mathbf{R} - \boldsymbol{\rho})] e^{iS(\mathbf{R}-\boldsymbol{\rho})-iS(\mathbf{R})} d\alpha \quad (49)$$

The electric field is therefore an analytic differential of the potential, which avoids spurious numerical instabilities [21]. The gradient is computed exactly using:

$$\nabla\Lambda_k = \frac{\partial\Lambda_k}{\partial s} \nabla s + \frac{\partial\Lambda_k}{\partial \theta} \nabla \theta \quad (50)$$

### 3.2.4 Gyro-averaging

We approximate with a four-point discrete sum the integrals over the gyroangle that are found in the charge assignment (48) and the gyro-averaged electric field (49). This has been shown [23] to be sufficient for perturbations with  $k_{\perp}\rho < 2$ . It is correct to the order of  $(k_{\perp}\rho_i)^2$ , the order at which (35) is correct.

Furthermore, the Larmor radius is approximated to lie in the poloidal plane rather than in the plane locally perpendicular to the magnetic field. The errors involved in the poloidal plane are of the order of  $(B_p/B_t)^2$ , which is usually small in tokamaks. As a consequence,  $\nabla_{\perp}$  and  $\mathbf{K}_{\perp}$  in the polarization density, Eq. (35), are approximated as the poloidal plane components of  $\nabla$  and  $\mathbf{K}$ , and the gyro-averages are computed in the poloidal plane.

### 3.2.5 Filtering

Filtering the potential can improve the numerical convergence of PIC schemes if it is used carefully. An efficient filter must use a representation where the signal is well separated from the noise. This is the case when the potential is Fourier transformed in the poloidal direction: the poloidal spectrum of unstable modes is localized around poloidal harmonics  $m \sim nq$ .

The potential is Fourier transformed in the poloidal direction and harmonics that are outside a user-selected range are eliminated. The filtered potential is then transformed back. In our simulations, we control the poloidal resolution with the range of poloidal harmonics; convergence with the filtering range is usually very fast. The number of poloidal grid points is kept large enough so that the highest poloidal harmonic allowed by the filter is well resolved. No filtering is done in the radial direction.

## 3.3 Spatial coordinate systems

The field quantities are computed in magnetic (i.e.  $(s, \theta)$ ) coordinates, because it allows an economical representation of the unstable modes and produces very good noise properties. This coordinate system has a singularity at  $s = 0$  that causes two difficulties for dealing with particles: first,  $\frac{d\theta}{dt}$  along guiding center trajectory diverges near the axis; second, finding the particle position  $\mathbf{x} = \mathbf{R} + \boldsymbol{\rho}$  from the guiding center position  $\mathbf{R}$  is difficult near the axis. These problems are circumvented by storing and evolving the particles in  $(R, Z)$  coordinates.

The transformations involved turned out to be computationally fast. For instance, the electric field from Eq. (49) is dealt with in the following way: for each of the four values of  $\alpha$  considered, the particle position  $\mathbf{x} = \mathbf{R} + \boldsymbol{\rho}(v_\perp, \alpha)$  is converted from  $(R, Z)$  to  $(s, \theta)$  coordinates;  $\Lambda(s, \theta)$  and its gradient can then be easily evaluated.

### 3.4 Computational cycle

The system is initialized by partitioning the phase space into  $N_p$  gyrocenter particles, the particle  $\nu$  representing a phase volume  $\xi_\nu$  and carrying an initial weight  $f_\nu = \xi_\nu f(\mathbf{R}_\nu, \mathbf{v}_\nu, t = 0)$ .

The charge assignment (48), which involves a four-point gyro-average deposition of the weight, provides a discrete charge on a  $(s, \theta)$  mesh. The finite element matrix problem (46) is then solved for the discrete potential. This allows the computation of the potential (43) and of the gyro-averaged electric field (49) at any point in space. The gyro-averaged electric field is given by a four-point average of the exact gradient of the electrostatic potential. The time-derivative of the particle weights (38), given by the computed electric field, and of the particle positions (31) and (32) are then known. This has to be evolved in time with an appropriate scheme; the one we use is described in Appendix (6.1). When the system evolves, the most unstable eigenmode of the system grows faster than any other mode and, after a finite amount of time, its amplitude dominates the perturbation. The spatial structure of the associated potential can then be reconstructed and the eigenmode frequency and growth rate can be measured during the time evolution.

Quadratic elements yield better results than linear elements; they provide a more accurate and less noisy answer in a computational time that is only slightly longer, or, conversely, a shorter computing time for a given accuracy.

### 3.5 Extraction of the ballooning phase factor

ITG modes can be unstable only when  $k_{\parallel} \ll k_{\perp}$ . Setting  $k_{\parallel} = \mathbf{h} \cdot \nabla \phi(s, \chi, \varphi) = 0$ , one can obtain a good estimate of the poloidal mode structure:

$$\phi(s, \theta, \varphi) = \hat{\phi}(s) \exp[-in\varphi + inq(s)\chi(s, \theta)], \quad (51)$$

$$\chi(s, \theta) = \frac{1}{q(s)} \int_0^\theta \frac{\mathbf{B} \cdot \nabla \varphi}{\mathbf{B} \cdot \nabla \theta'} d\theta', \quad (52)$$

where  $\hat{\phi}(s)$  is a free complex function;  $\chi$  is the “straight-field-line” angle [24].

As high- $n$  modes have a fine poloidal structure, their numerical treatment demands both a large number of poloidal grid points and a small time step  $\Delta t$ . Indeed, integration

accuracy and stability require  $\Delta t$  to be smaller than the time it takes a particle to cross one poloidal wavelength. This translates into a maximum time step which is inversely proportional to  $n$ . This limitation at high  $n$  can be overcome by taking advantage of the approximate knowledge given by Eq. (51), similarly to what was done in [25]. Let us redefine transformed quantities by redefining the function  $\Sigma$  in Eq. (26):

$$\Sigma(s, \theta) = nq(s)\chi(s, \theta). \quad (53)$$

With this, the transformed potential (25) corresponding to (51) reduces to  $\tilde{\phi}(s, \varphi, \theta) = \hat{\phi}(s)$  and does not vary poloidally: the structure corresponding to  $k_{\parallel} = 0$  (or, in other words, the ballooning phase factor) has been extracted analytically. In unstable ITG modes,  $k_{\parallel}$  is small, but non-zero, and the extracted quantities vary in the poloidal direction, but only slowly, even at high  $n$ . This transformation is closely related to that which leads to the ballooning approximation.

The transformed quantities  $\tilde{\phi}$  and  $\tilde{f}$  are not periodic at the boundary  $\theta = 0/2\pi$  for non-integer values of  $nq(s)$ . To avoid the technically cumbersome jump conditions involved, we consider a simpler choice for  $\Sigma(s, \theta)$ :

$$\Sigma(s, \theta) = m_0\chi(s_0, \theta) \quad (54)$$

where  $m_0$  is an integer close to  $nq(s_0)$  and  $s_0$  is the expected radial position of the mode. The equations derived in previous sections are valid for any function  $\Sigma$ . No new approximations are involved.

Figure (3) shows the potential from a typical medium- $n$  ( $n = 24$ ) simulation without extraction. The same physical case is shown in Fig. (4), using the extraction with  $m_0 = -37$ . The frequency and growth rate agree within 1% and 5% respectively, which is within the uncertainties resulting from the numerical resolution. The number of poloidal grid points needed is reduced, which in turn reduces the numerical noise and the number of particles required. The simulation time step can be greatly increased because the poloidal wavelength of the transformed quantities is large and independent of  $n$ . As a consequence, the extraction decreases the cost of large  $n$  simulations by two orders of magnitude while improving the precision of the results.

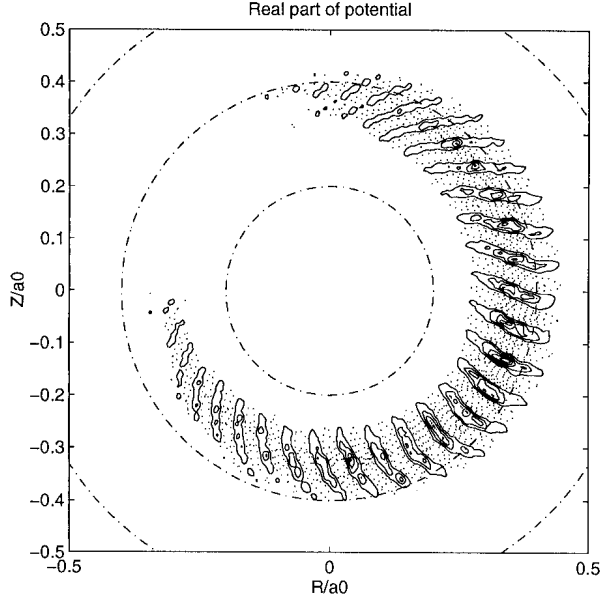


Figure 3: Potential  $\phi(s, \theta)$  obtained in a simulation without extraction, i.e. with  $\Sigma(s, \theta) = 0$ , using 128 poloidal grid points. The frequency and growth rate obtained are  $\omega = 627$  kHz and  $\gamma = 233$  kHz.

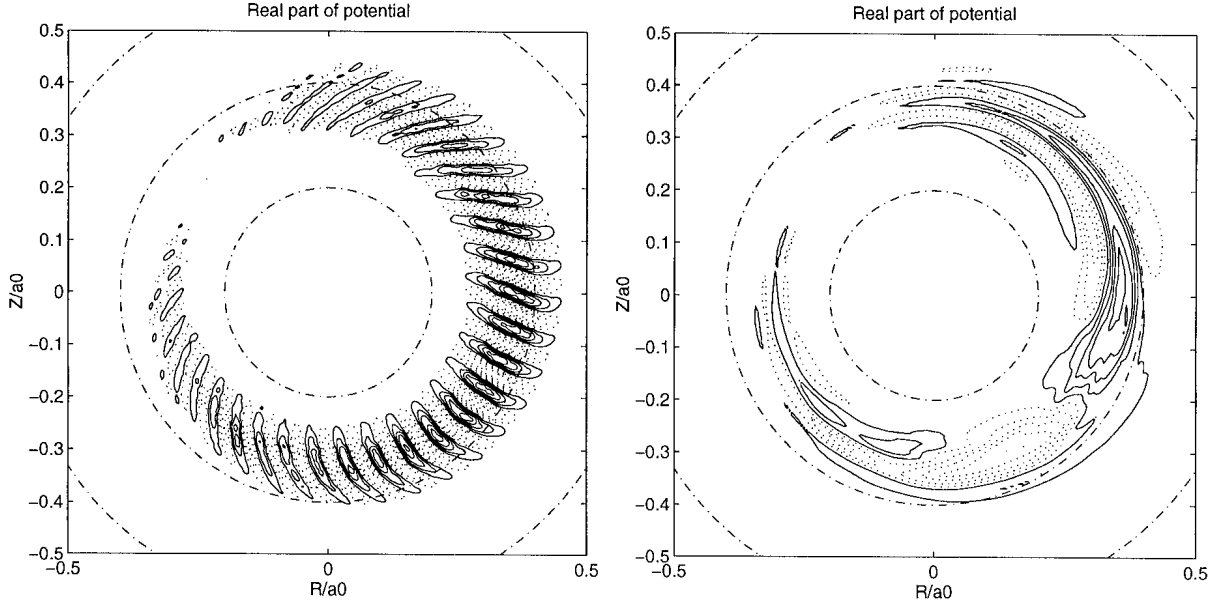


Figure 4: Simulation with extraction of  $\Sigma(s, \theta) = m_0 \chi(s_0, \theta)$ ,  $m_0 = -37$ , using 32 poloidal grid points. The transformed potential  $\phi(s, \theta)$  (right) which is discretized using the finite elements, varies very slowly compared to the potential  $\phi(s, \theta) = \tilde{\phi}(s, \theta)e^{i\Sigma}$  (left). The frequency and growth rate obtained are  $\omega = 634$  kHz and  $\gamma = 243$  kHz. The time step is 24 times larger than in the simulation shown in Fig. (3), and both the noise and the number of poloidal grid points are reduced. The extraction decreases the cost of large  $n$  simulations by two orders of magnitude while improving the precision of the results.

## 4 Validation

The code is validated in three different ways.

First, we check the power consistency of the simulations: the work of the ions in the electric field must be equal to the time-derivative of the field energy. These quantities are calculated during the evolution and are compared.

Second, we show that the simulations converge to a unique solution when the numerical resolution is enhanced.

Third, we compare the results with those of other codes that solve the same equations.

These three validations are successful; they have been made on realistic cases of physical interest. We believe that together, they show that the model is implemented correctly, that the numerical procedure converges well to the physical solution of the equations solved and that the results of the code are valid.

### 4.1 Power consistency

The original nonlinear equations conserve energy in time; this cannot be checked directly in a linear simulation, since the ion kinetic energy depends on the perturbed particle trajectories, which are not known. However, the time-derivative of the kinetic energy can be written in the form of the work done by the particles in the electric field, and then computed. It can then be compared to the numerical time-derivative of the field energy, which is directly accessible. The field energy is given by:

$$E_{\text{field}} = \frac{q_i}{2} \int \left[ \frac{n_0 e}{T_e} \phi^2 + \frac{n_0}{B\Omega} \mathbf{E}_\perp^2 \right] d\mathbf{x} \quad (55)$$

The first term is related to the adiabatic electron response and the second to the ion polarization drift. For notation compactness,  $\phi$ ,  $f$  and  $\mathbf{E}$  refer here to the quantities before the transformations (24) and (25). Using Liouville's theorem as in [16] and the field equation (35), one can show that:

$$\frac{dE_{\text{field}}}{dt} = -\frac{dE_{\text{kin}}}{dt} = q_i \int f \mathbf{v}_{gc} \cdot \langle \mathbf{E} \rangle d\mathbf{R} d\mathbf{v} \quad (56)$$

where  $\frac{d}{dt}E_{\text{kin}}$  is the power transfer from the particles to the electric field,  $\mathbf{v}_{gc} = \frac{d}{dt}\mathbf{R}$  is the guiding center velocity from Eq. (31) and  $\langle \mathbf{E} \rangle$  is the gyro-averaged electric field.

When one eigenmode only is present in the simulation, its growth rate  $\gamma$  is given by the logarithmic time-derivative of the field energy:

$$\gamma = \frac{1}{2E_{\text{field}}} \frac{dE_{\text{field}}}{dt}, \quad \text{or} \quad (57)$$

$$\gamma = -\frac{1}{2E_{\text{field}}} q_i \int f \mathbf{v}_{gc} \cdot \langle \mathbf{E} \rangle d\mathbf{R} d\mathbf{v} \quad (58)$$

Equation (58) therefore provides an instantaneous measurement of the growth rate. The destabilizing mechanism can be revealed by decomposing the growth rate (58) into a sum of the various contributions of the guiding center velocity in Eq. (56). For instance, one can distinguish the slab ITG mechanism [26]  $\gamma \sim \int f v_{\parallel} \mathbf{h} \cdot \langle \mathbf{E} \rangle$  from the toroidal ITG mechanism [27]  $\gamma \sim \int f \mathbf{v}_{gc}^{pol} \cdot \langle \mathbf{E} \rangle$ , where  $\mathbf{v}_{gc}^{pol}$  is the poloidal drift guiding velocity.

In Fig. (5), left, one can compare the growths rates computed with Eqs. (58) and (57) the time-derivative being computed with finite difference. Their relative error is shown on the right. The two simulations shown (top and bottom) differ by the number of particles used only. When there are enough particles, after an initial transient period, the error reduces to the order of one percent. It decreases when the numerical resolution is enhanced, e.g. when reducing the time step. The numerical scheme does not guarantee intrinsically the power consistency (56). Since the powers compared are measured from two very different quantities, (the time derivative of the potential and an instantaneous integral over the particles), the comparison provides a good measurement of the quality of a simulation. It checks both whether the physical model is implemented correctly and whether the numerical resolution is adequate, which is the case in the example shown within an uncertainty of less than two percent in the growth rate, Fig. (5), bottom right.

## 4.2 Convergence studies

There are a number of numerical parameters which define the resolution with which the model equations are solved. The phase space discretization of the distribution function is determined by the number of particles and the phase space discretization limits (range in radial variable  $s$  and the maximum discretized velocity). The discretization of the



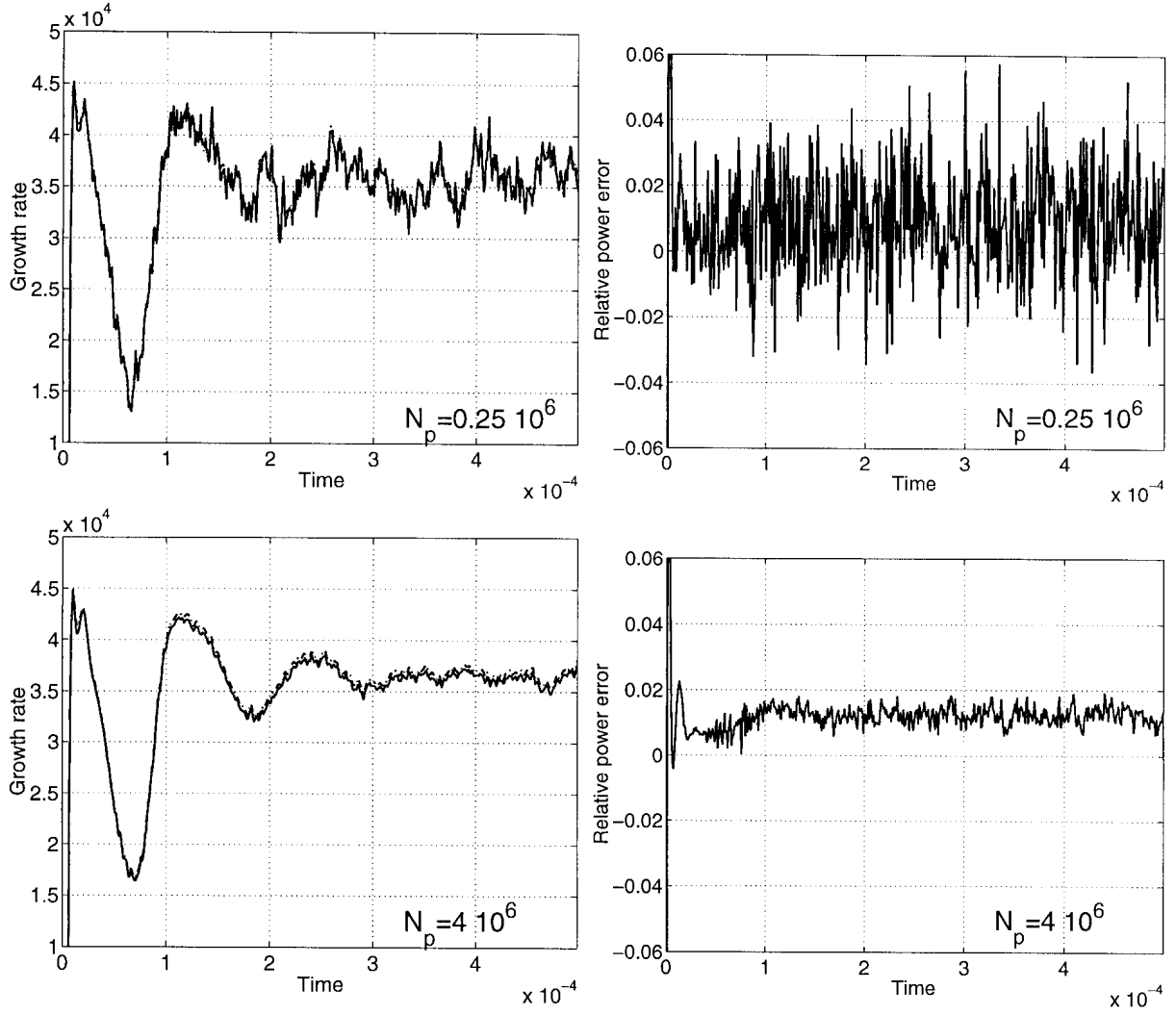


Figure 5: Left: Normalized power transfer from particles to field, Eq. (58) (plain line) and variation of field energy, Eq. (57) (dotted line), the time-derivative being computed by finite difference between time steps. The difference is so small that the curves are difficult to distinguish on the present scale. Right: relative error on power transfer. Top: simulation with one quarter of a million particles, bottom: the same case with four million particles.

potential is controlled by the number of poloidal and radial mesh points as well as the range in poloidal harmonics that are not filtered out. The magnetic field is stored on a grid (see Appendix 6.2) whose resolution must be adequate. The simulation timestep sets the time resolution, and, finally, the total simulation time must be long enough to allow the most unstable mode to grow to a dominant amplitude.

All these parameters have been checked to provide convergence, i.e. above a certain resolution, their value does not influence significantly the code results. We show two convergence tests here. First, we show the convergence of the growth rate obtained with an increasing number of particles. Second, the spatial structure of the numerical solution to the field equation is shown to converge to the exact solution as the mesh spacing to the fourth power when we use quadratic finite elements.

#### **4.2.1 Convergence with the number of particles**

We show here the convergence of the growth rate with the number of particles. The growth rate is shown versus the number of particles in Fig. (6a). The full line shows the growth rate averaged over a time span after the transients. The growth rate converges well to a fixed value; for this case, a quarter of a million particles is enough to produce a result accurate to the order of a percent, which is more than enough for our purpose. The final results are usually produced using one million particles for additional safety. The standard deviation, shown by the crosses, shows the typical error in the instantaneous growth rate. The relative error in powers, Fig. (6b), converges to a fixed value of the order of one percent. It can be reduced further by enhancing the numerical resolution associated with other numerical parameters.

#### **4.2.2 Convergence of the potential with mesh spacing**

We measure here the accuracy of the numerical solution of the field equation (35). An analytic solution is found for a particular perturbed density; this density is used as the right-hand-side of Eq. (35). The field equation is solved and the discrete potential obtained is compared to the analytic solution. The error obtained is shown in Fig. 7 as a function of the number of radial grid points: it decreases as the mesh spacing to the

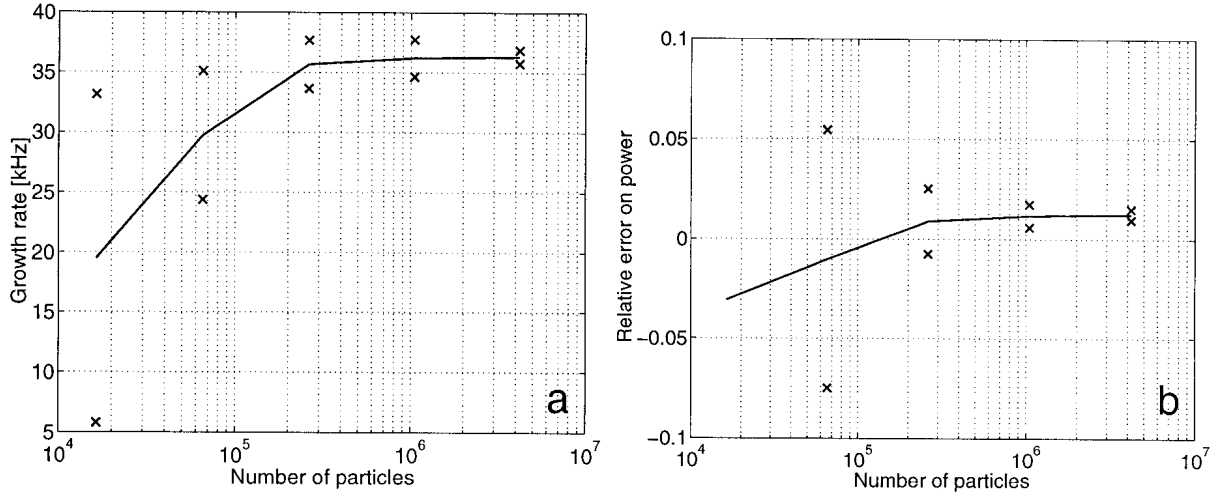


Figure 6: *Convergence with the number of particles: growth rate (a) and relative power error (b). The crosses are one standard deviation away from the time-average, shown by the full line.*

fourth power for second order spline finite elements, an excellent convergence property. The analytic solution used is maximum at the  $s=0$  origin, this test therefore shows that the unicity condition is implemented correctly. For quadratic finite elements, 3-5 points per wavelengths ensure that the results are converged with respect to the mesh spacing.

### 4.3 Comparison with other codes

The code was validated against two other codes: the global eigenvalue code [28] and the nonlinear code [12], during the linear growth phase. Our comparison case has a major radius  $R_0 = 1.2$  m, a minor radius  $a = .2$  m, an average Larmor radius  $\rho = 3.2$  mm, a parabolic safety factor  $q = [1.25 \dots 4.25]$  and a flat density. The steepest temperature gradient is at  $s = .5$  where  $L_T/R = .13$ . The growth rate and frequencies of the most unstable mode are compared on Fig. (8). The growth rate from the eigenvalue code differ at low  $n$  because it does not take the trapped ions into account, and the frequency (at low  $n$ ) is comparable to the trapped ion bounce frequency. The nonlinear code results have a large uncertainty in the frequency related to the method of measurement. The field equation solved in this code is approximate (the coefficients of the equation are assumed constant in space): this might explain the differences in growth rate observed at low  $n$ .

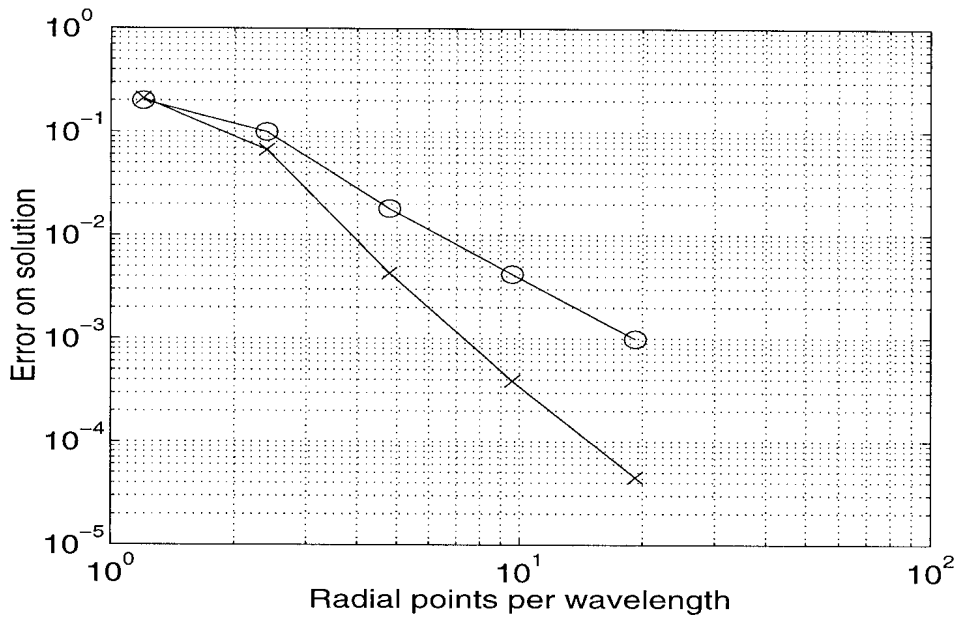


Figure 7: *Convergence of the potential with the number of radial grid points. The number of poloidal grid points varies proportionally. (o): linear finite elements; the error converges with the number of radial points squared. (x): second order finite elements; the error converges with the number of radial points to the fourth power.*

Both the eigenvalue code and the nonlinear code include Larmor radius effects to all order in  $(k_{\perp}\rho)$ , corresponding to Eq. (20), while the present code uses an expansion in Larmor radius leading to Eq. (21). This approximation breaks down at high  $n$  ( $k_{\theta}\rho \approx 1$ , here at  $n \approx 15$ ), but seems to have little effect here, since the results of the three codes agree well, at least for the growth rate.

Overall, though, the results are in good agreement, and the validation is successful.

The code was also benchmarked qualitatively against the nonlinear code [11] in a version that uses a full MHD equilibrium. More benchmarking was done against the eigenvalue code and reported in [28]; the latter code has been benchmarked successfully [13] against a ballooning code.

## 5 Conclusions

We have developed a global gyrokinetic simulation code to address the problem of the stability of electrostatic perturbations in realistic toroidal equilibria. A time-evolution

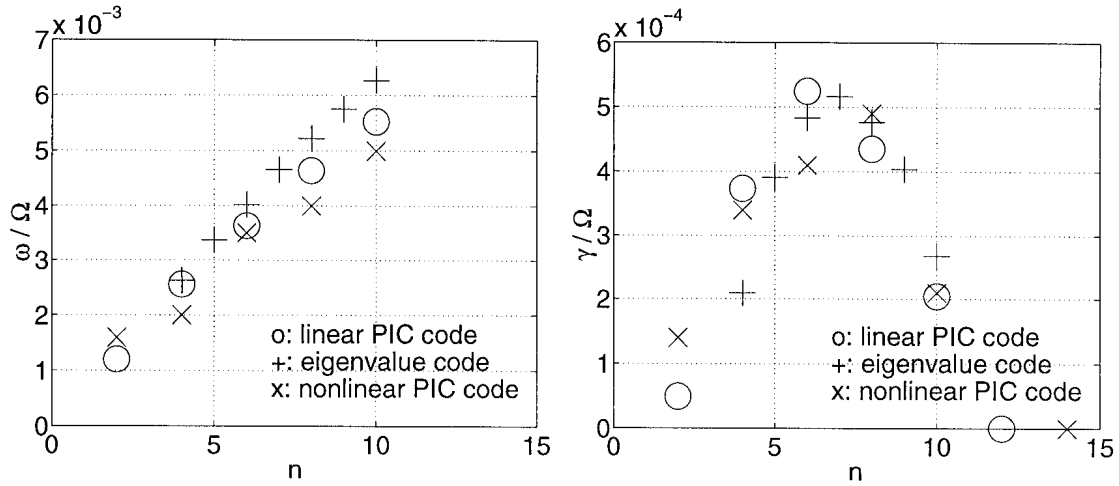


Figure 8: *Frequency(left) and growth rate(right) obtained with the three codes compared, versus the toroidal mode number  $n$ . Positive frequencies refer to modes propagating in the ion diamagnetic direction.*

approach allows us to find efficiently the most unstable mode of the system. The finite element formulation allows to use magnetic coordinates for the representation of the potential and provides excellent convergence properties. The fast-varying poloidal  $k_{\parallel} = 0$  structure (or ballooning phase factor) was extracted from the equations without loss of generality for the global solution; we then solve for the slowly-varying envelope. This reduces the computing time by up to two orders of magnitude and allows to treat all values of the toroidal mode number  $n$  without approximation. The code has been carefully validated, both with convergence tests and by comparison with other codes. All toroidal wavelengths, all plasma sizes, shapes and pressures can be handled routinely, often with less than a million particles. With this code, we can perform global, kinetic calculations to study, Fig. (9), the regimes of toroidal ITG, trapped-ion mode and slab ITG, as well as their transitions. The code has been applied to study finite pressure effects on ITG modes [15] [17] [18].

Future development will be aimed at improving the physical model; we are currently including the dynamics of the trapped electrons, which is known to be important, especially at small values of  $\eta$  [13]. Other interesting improvements are the inclusion of plasma flow, electromagnetic perturbations and collisionality. Extensions of the code towards other 2D geometries (e.g. helical symmetry) have been started.

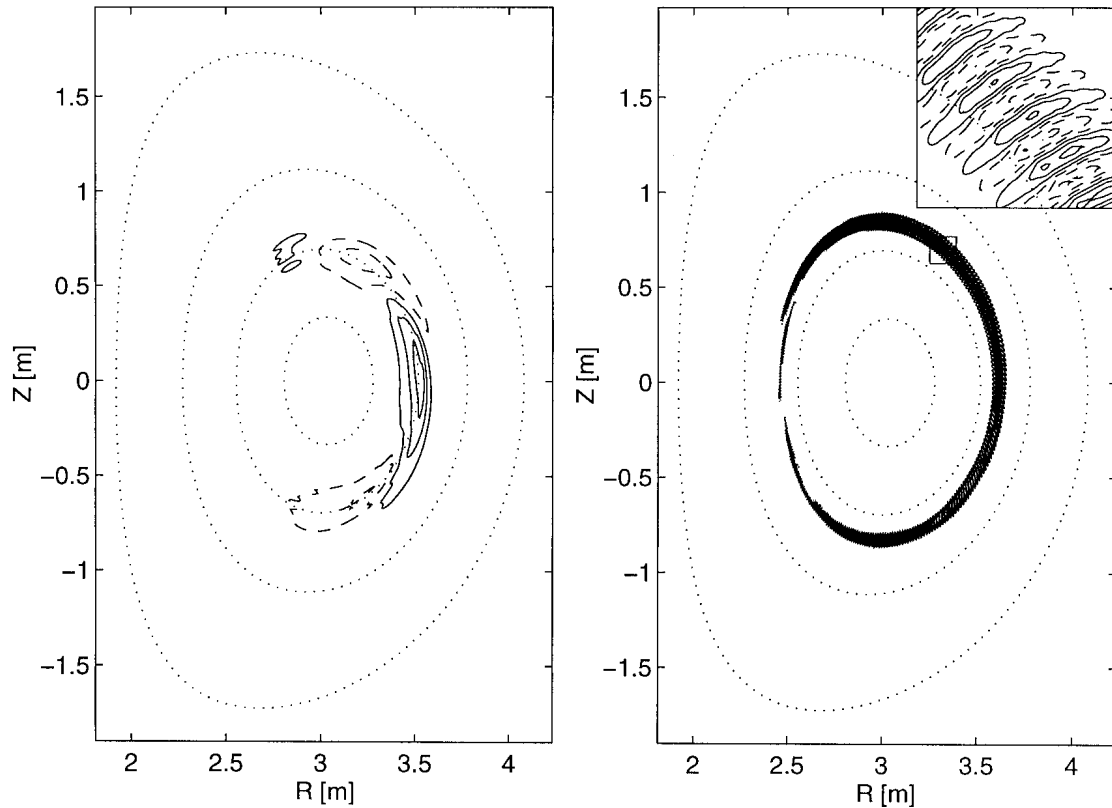


Figure 9: *Low- $\beta$  JET-size equilibria with major radius  $R_0=3m$ , minor radius  $a=1.08m$ ,  $T_i = 16$  keV at plasma center. At the mode approximate radial location,  $q = 1.5$ ,  $\eta_i=4$ ,  $R_0/L_T=18$  and  $T_i = T_e = 4$  keV. Left:  $n=2$ , a trapped ion mode. Right:  $n=48$ , a toroidal ITG mode. Simulation with 1 million particles and  $32 \times 32$  grid points. The transition between the trapped-ion and toroidal ITG regimes occurs around  $n=10$ .*

## Acknowledgements

This research was supported in part by both the Cray/EPFL Parallel Application Technology Program and the Swiss National Science Foundation. The computations have been performed on the Cray-T3D of the Ecole Polytechnique Fédérale in Lausanne and on the Cray-T3D of the Jet Propulsion Laboratory, whose access was provided by NASA's Office of Mission to Planet Earth, Office of Aeronautics, and Office of Space Science. We thank R. Sydora for providing us the comparison data for Fig. (8) and both R. Sydora and S. Parker for useful discussions.

## 6 Appendices

### 6.1 Time integration scheme

We describe here the numerical scheme that is used to integrate the equations over time. The superscript indicates the time step number. Starting from the weights  $f^n$  at time  $t^n$ , one obtains  $f^{n+1}$  at time  $t^{n+1}$  in a predictor-corrector procedure.

Half step forward:

- (a) Compute  $\phi^n$  from  $f^n$ , Eq. (46)
- (b) Evolve  $f^n$  to  $f^{n+\frac{1}{2}}$  using  $\mathcal{T}(\phi^n)$ , Eq. (38)
- (c) Evolve  $(R, Z, v_{\parallel}, v_{\perp})^n$  to  $(R, Z, v_{\parallel}, v_{\perp})^{n+\frac{1}{2}}$ , Eqs. (31),(32)

Time-centered full step:

- (d) Compute  $\phi^{n+\frac{1}{2}}$  from  $f^{n+\frac{1}{2}}$
- (e) Evolve  $f^n$  to  $f^{n+1}$  using  $\mathcal{T}(\phi^{n+\frac{1}{2}})$
- (f) Evolve  $(R, Z, v_{\parallel}, v_{\perp})^{n+\frac{1}{2}}$  to  $(R, Z, v_{\parallel}, v_{\perp})^{n+1}$

Steps (c) and (f) are done using a sophisticated Burlisch-Stoer scheme [22] which guarantees a very precise integration, even for large time steps. Steps (b) and (e) need special care if large time steps are to be taken when  $\Sigma(s, \theta)$  has fast spatial variations. In that case,  $\frac{dS}{dt}$  in Eq. (33) is large and induces rapid phase variations in  $f(t)$  during one time step, up to many times  $2\pi$  when the  $k_{\parallel} = 0$  extraction is used at high  $n$ . A good integration scheme for arbitrary values of  $\frac{dS}{dt}\Delta t$  is obtained by splitting the time step and integrating the fast variation analytically:

$$\begin{aligned}
 \text{(A)} \quad f_{*} &= f^t + \mathcal{T} \frac{\Delta t}{2}, \\
 \text{(B)} \quad f_{**} &= f_{*} e^{-i \frac{dS}{dt} \Delta t}, \\
 \text{(C)} \quad f^{t+\Delta t} &= f_{**} + \mathcal{T} \frac{\Delta t}{2}.
 \end{aligned}$$

where  $\Delta t = t^{n+1} - t^n$  for step (e) and half that value for step (b) above. This scheme is exact when  $\frac{dS}{dt}$  and  $\mathcal{T}$  do not vary in time.

## 6.2 Coupling with the MHD equilibrium solver CHEASE

The functions  $\Psi$  and  $T(\Psi)$  that appear in the expression for the magnetic field, Eq. (1), are given either by an ad-hoc function or by a numerical solution of the Grad-Shafranov equation computed by the code CHEASE [14].

In an interface developed for our gyrokinetic code, the quantities  $\Psi$ ,  $\frac{\partial \Psi}{\partial R}$ ,  $\frac{\partial \Psi}{\partial Z}$ ,  $\frac{\partial^2 \Psi}{\partial R^2}$ ,  $\frac{\partial^2 \Psi}{\partial Z^2}$ ,  $\frac{\partial^2 \Psi}{\partial R \partial Z}$ ,  $T$ , and  $\frac{\partial T}{\partial \Psi}$ , are interpolated using cubic splines on a  $(R, Z)$  mesh which encloses the plasma boundary. The quantities appearing in the gyrokinetic equations, such as  $\frac{1}{B^3} \mathbf{B} \times \nabla B$  are pre-computed in the gyrokinetic code and stored on the same mesh. They are retrieved and interpolated linearly when needed.

Alternatively,  $\Psi(R, Z)$  and  $T(\Psi)$  will be given by ad-hoc functions, producing a circular equilibrium without Shafranov shift and with a prescribed safety factor profile:

$$r(R, Z) = \sqrt{(R - R_M)^2 + Z^2} \quad (59)$$

$$\Psi(r) = \int_0^r \frac{r' B_0}{q(r')} dr' \quad (60)$$

$$q(r) = q_0 + (q_s - q_0)(r/a)^{p_q} \quad (61)$$

$$T(\Psi) = B_0 R_0 \quad (62)$$

where  $a$  is the plasma small radius and  $q(r)$  is the approximate safety factor which depends on the parameters  $q_0$ ,  $q_s$  and  $p_q$ .

## 6.3 Parallelization on the T3D

Most of the computing time is spent on evolving the distribution function, i.e. on dealing with particles. This leads us to divide the particles among the processors, thus spreading among processors the most computing-intensive calculations.

The charge assignment is done privately: each processor computes the charge density corresponding to the particles it stores. The private densities are then summed across the processors, each processor getting as a result the charge corresponding to all the particles. The back-substitution for the solution of the field equation is duplicated on every processor, as it is very fast.



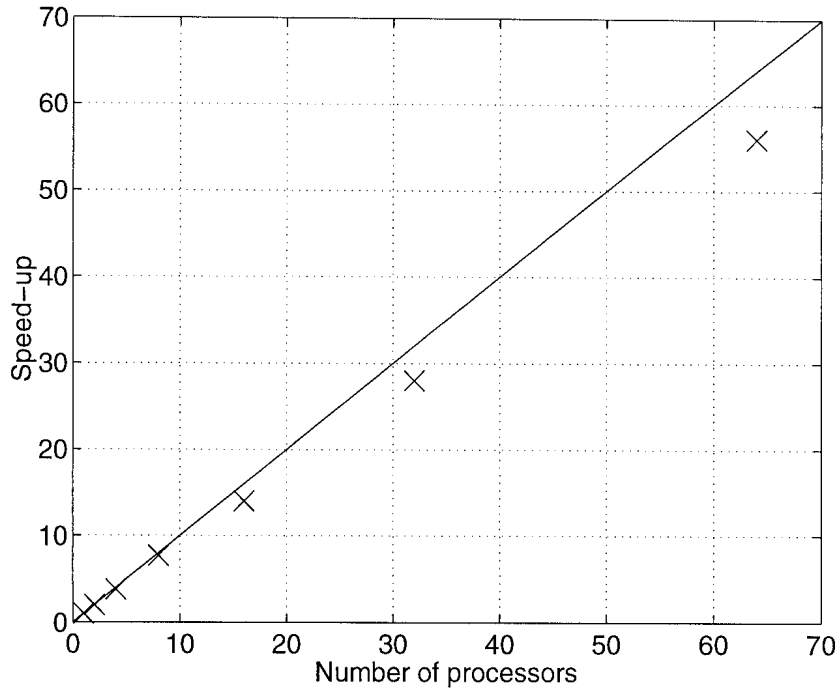


Figure 10: *Speed-up obtained on the T3D for a small size run, 262000 particles and 30x30 grid. The computing speed scales up very well to 64 processors.*

Figure (10) shows the ratio of execution time obtained to the execution time on one processor, or speed-up, as a function of the number of processors. The computing time decreases linearly with the number of processors up to 64 processors for typical numerical parameters, and up to 256 processors for larger physical cases. The performance obtained is around 15 Mflops per processor. Typical well-converged cases such as shown on Fig. (9) takes around one hour on a 64-processor configuration, but a rough growth rate, within 10%-30%, can be obtained ten times faster.

## References

- [1] R. D. Hazeltine, Phys. Fluids B **2**, 7 (1990).
- [2] G. Rewoldt, W. M. Tang, and M. S. Chance, Phys. Fluids **25**, 480 (1982).
- [3] X. Q. Xu and N. M. Rosenbluth, Phys. Fluids B **3**, 627 (1991).
- [4] M. Kotschenreuther, G. Rewoldt, and W. M. Tang, Comp. Phys. Comm. **88**, 128 (1995).
- [5] R. J. Fonck, G. Cosby, R. D. Durst, S. F. Paul, N. Bretz, S. Scott, E. Synakowski, and G. Taylor, Phys. Rev. Lett. **70**, 3736 (1993).
- [6] R. Durst, R. J. Fonck, J. S. Kim, S. F. Paul, N. Bretz, C. Bush, Z. Chang, and R. Hulse, Phys. Rev. Lett. **71**, 3135 (1993).
- [7] R. Marchand, W. Tang, and G. Rewoldt, Phys. Fluids **23**, 1164 (1980).
- [8] W. M. Tang and G. Rewoldt, Phys. Fluids B **5**, 2451 (1992).
- [9] M. Artun, W. M. Tang, and G. Rewoldt, Phys. Plasmas **2**, 3384 (1995).
- [10] W. W. Lee, Phys. Fluids **26**, 556 (1983).
- [11] S. E. Parker, W. W. Lee, and R. A. Santoro, Phys. Rev. Letters **71**, 2042 (1993).
- [12] R. D. Sydora, V. K. Decyk, and J. M. Dawson, Plasma Phys. Contol. Fusion **38**, A281 (1996).
- [13] S. Brunner, Ph.D. thesis, Ecole polytechnique Fédérale de Lausanne, Switzerland, thesis 1701, 1997.
- [14] H. Lütjens, A. Bondeson, and O. Sauter, Comput. Phys. Commun. **97**, 219 (1996).
- [15] M. Fivaz, Ph.D. thesis, Ecole polytechnique Fédérale de Lausanne, Switzerland, thesis 1692, 1997.
- [16] T. S. Hahm, Phys. Fluids **31**, 2670 (1988).
- [17] M. Fivaz, T. Tran, K. Appert, J. Vaclavik, and S. E. Parker, Phys. Rev. Lett. **78**, 3471 (1997).
- [18] M. Fivaz, O. Sauter, K. Appert, T. M. Tran, and J. Vaclavik, to be submitted to Physics of Plasmas, 1997.
- [19] C. K. Birdsall and A. B. Langdon, *Plasma Physics via Computer Simulations Using Particles* (McGraw-Hill, New York, 1985).
- [20] J. W. Eastwood, Comput. Phys. Comm. **64**, 252 (1991).
- [21] J. A. Byers, A. M. Dimits, Y. Matsuda, and A. B. Langdon, Journal Comput. Phys. **115**, 352 (1994).

- [22] W. H. Press, B. P. Flannery, S. A. Teukolsky, and W. Vetterling, *Numerical Recipes* (Cambridge University Press, 32 East 57th Street, New York, NY 10022, USA, 1986).
- [23] W. W. Lee, *Journal of Comp. Phys.* **72**, 243 (1987).
- [24] W. D. D’haeseleer, W. N. G. Hitchon, J. D. Callen, and J. L. Shohet, *Flux coordinates and magnetic field structure* (Springer-Verlag, New York, 1991).
- [25] R. Gruber, F. Troyon, D. Berger, L. C. Bernard, S. Rousset, R. Schreiber, W. Kerner, W. Schneider, and K. V. Roberts, *Comput. Phys. Commun.* **21**, 323 (1981).
- [26] A. B. Mikhailovskii, *Theory of plasma instabilities, Vol. 2* (Consultant Bureau, New York, 1974).
- [27] W. Horton, *Phys. Fluids* **24**, 1077 (1983).
- [28] S. Brunner, M. Fivaz, J. Vaclavik, T. M. Tran, and K. Appert, in *Theory of fusion plasmas, Int. Workshop, Varenna, August 1996* (Editrice Compositori, Società Italiana di Fisica, Bologna, 1997), p. 101.